ACS APPLIED MATERIALS & INTERFACES

Research Article

www.acsami.org

# High-Performance Asymmetric Supercapacitor Based on Nanoarchitectured Polyaniline/Graphene/Carbon Nanotube and Activated Graphene Electrodes

Jiali Shen, Chongyang Yang, Xingwei Li, and Gengchao Wang*

Shanghai Key Laboratory of Advanced Polymeric Materials, Key Laboratory for Ultrafine Materials of Ministry of Education, School of Materials Science and Engineering, East China University of Science and Technology, Shanghai 200237, People's Republic of China

Supporting Information

**ABSTRACT:** Hierarchical sulfonated graphene nanosheet/carboxylated multiwalled carbon nanotube/polyaniline (sGNS/cMWCNT/PANI) nanocomposites were synthesized through an interfacial polymerization method. Activated porous graphene (aGNS) was prepared by combining chemical foaming, thermal reduction, and KOH activation. Furthermore, we have successfully fabricated an asymmetric supercapacitor (ASC) using sGNS/cMWCNT/PANI and aGNS as the positive and negative electrodes, respectively. Because of its unique structure, high capacitive performance, and complementary potential window, the ASC device can be cycled reversibly at a cell voltage of 1.6 V in a 1 M $H_2SO_4$ aqueous electrolyte, delivering a high energy density of 20.5 Wh $kg^{-1}$ at a power density of 25 kW $kg^{-1}$. Moreover, the ASC device also exhibits a superior long cycle life with 91% retention of the initial specific capacitance after 5000 cycles.

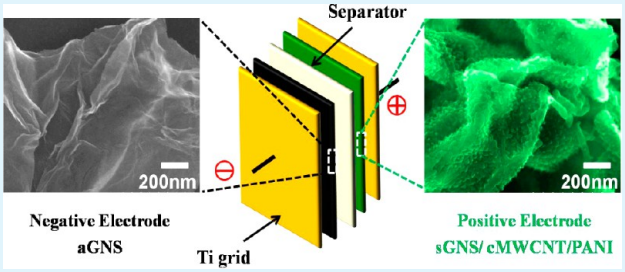


**KEYWORDS:** *nanostructured polyaniline, graphene, carbon nanotubes, interfacial polymerization, activation, asymmetric supercapacitor*

## INTRODUCTION

Supercapacitors are vital to meet the future energy-storage demand in hybrid electric vehicles, memory back-up systems, and industrial energy management owing to their high power density, long cycle life, and fast charging/discharging processes.[1−3] However, they deliver lower energy density, which greatly restricts their application.[4] According to the equation $E = {}^1/_2CV^2$, an effective way is to develop hierarchical nanostructured or nanoporous materials to promote the specific capacitance of electrodes[5−8] and another way is to explore asymmetric supercapacitors (ASCs), which integrate the different potential windows of capacitive and pseudocapacitive electrodes to increase the cell voltage.[9−12] A variety of ASC devices such as $Ni(OH)_2$//C,[13,14] $M_xO_y$ (M = Mn, Ni, Fe, V, etc.)//C,[15−19] $LiM_xO_y$//C (M = Mn, Co, etc.),[20,21] and C//$Li_4Ti_5O_{12}$[22] have been developed. However, ASCs based on conducting polymers were rarely reported.

Polyaniline (PANI) is a promising positive electrode material because of its low cost, ease of synthesis, and relatively high electrical conductivity.[23] However, PANI exhibits poor rate capability, inferior cycling stability, and a narrow potential window. Previous reports have described that coupling nanostructured PANI to carbonaceous materials can improve the utilization of PANI and provide a short transport path for ion and electron.[23−30] Up to now, numerous composites of graphene nanosheet/PANI (GNS/PANI),[26,27,31−34] carbon nanotube/PANI (CNT/PANI),[28,29,35−38] and GNS/CNT/PANI[39−41] have been explored, among which hierarchical structured GNS/CNT/PANI composites remarkably facilitate the charge transport and increase the accessible surface for PANI deposition.[39] To further increase the electrochemical performance of PANI, a homogeneous nanometer-sized and well-ordered structure must be considered.[23,42]

On the other hand, an appropriate negative electrode is indispensable to achieve a good rate performance at a high energy density.[5,15,43] Two-dimensional GNS has been recognized as an ideal candidate because of its large surface area, high electrical conductivity, superior mechanical property, and relatively wide potential window.[44−46] However, to overcome the restacking and aggregation of GNS caused by van der Waals interaction, modification or activation is necessary to enhance the accessible surface.[47−50] More recently, Kaner et al. produced a flexible graphene film with a specific surface area of 1520 $m^2$ $g^{-1}$ through laser scribing.[8] Murali et al. developed highly porous graphene with Brunauer−Emmett−Teller (BET) surface area of 3100 $m^2$ $g^{-1}$ based on KOH activation of microwave-exfoliated graphite oxide (MEGO).[7]

Received: May 19, 2013
Accepted: August 9, 2013
Published: August 9, 2013

   dx.doi.org/10.1021/am4028235 | ACS Appl. Mater. Interfaces 2013, 5, 8467−8476

**Scheme 1. Schematic Illustration of the Fabricated ASC Device Based on a sGNS/cWMCNT/PANI Composite as the Positive Electrode and aGNS as the Negative Electrode in 1 M $H_2SO_4$ Electrolyte**

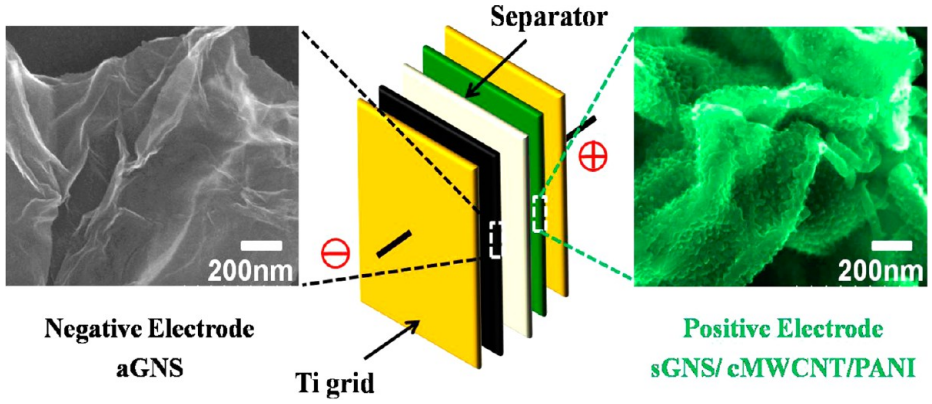


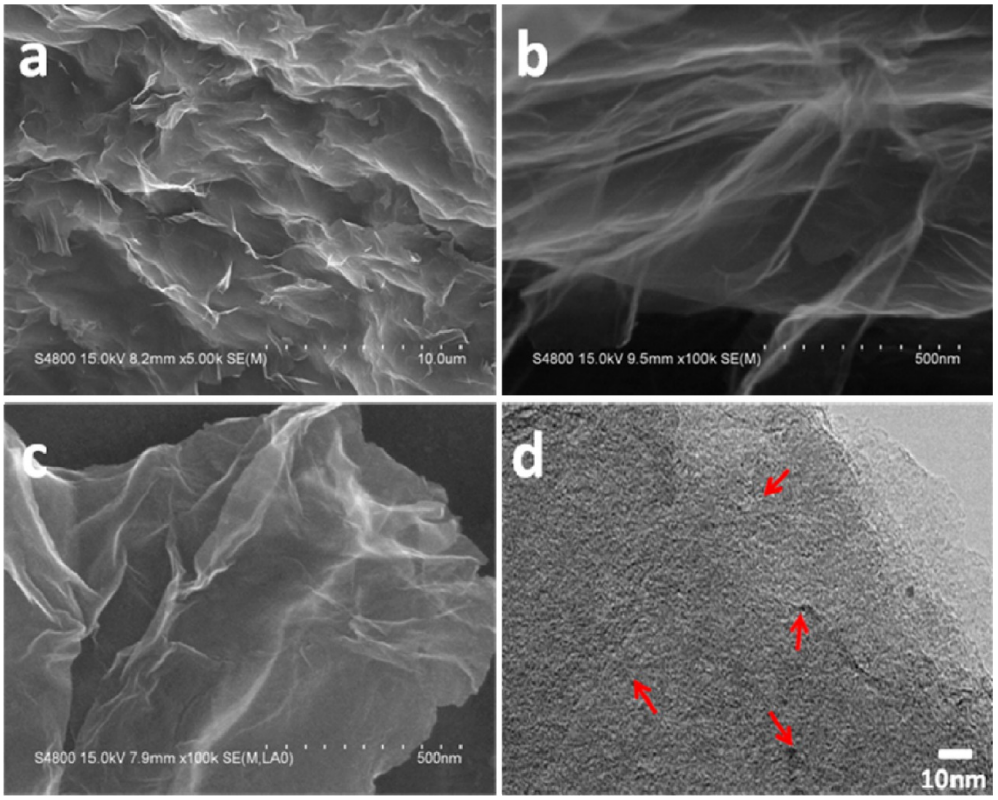


**Figure 1.** FESEM images of (a and b) GNS and (c) aGNS. (d) HRTEM image of aGNS.

In this study, we developed a novel ASC device based on a sulfonated graphene nanosheet/carboxylated multiwalled carbon nanotube/polyaniline (sGNS/cMWCNT/PANI) nanocomposite as the positive electrode and activated porous graphene (aGNS) as the negative electrode in a $H_2SO_4$ aqueous electrolyte (Scheme 1). The sGNS/cMWCNT/PANI nanocomposite was synthesized by interfacial polymerization, and aGNS was prepared by thermal reduction assisted with SA and activation with KOH. The as-prepared ASC device obtained stable electrochemical behavior in a 1.6 V potential window and displayed a maximum energy density of 41.5 Wh $kg^{-1}$, which was much higher than that of symmetric supercapacitors based on sGNS/cMWCNT/PANI//sGNS/cMWCNT/PANI (21.1 kW $kg^{-1}$) and aGNS//aGNS (6.5 kW $kg^{-1}$). Meanwhile, the ASC device also exhibited a superior long cycle life with only 9% performance loss after 5000 cycles.

## EXPERIMENTAL SECTION

**Preparation of aGNS.** Graphene oxide (GO) was synthesized using the modified Hummers method.[51] aGNS derived from GO was synthesized by thermal reduction assisted by a foaming agent and activation with KOH.[7,52] Briefly, GO (0.5 g) was dispersed in an ethanol solution of 0.5 g of salicylic acid (SA) to obtain a uniform slurry. The superfluous SA was removed by filtering the mixture, followed by drying at 60 °C overnight. The dry GO/SA mixture was first heated at 200 °C for 15 min, and then the temperature was ramped at 10 °C $min^{-1}$ to 500 °C and held there for 2 h under a mixed gas flow of hydrogen and argon (20:80, v/v) to obtain GNS. Finally, GNS and KOH were mixed with a weight ratio of 1:6 and heated to 800 °C at a ramp of 10 °C $min^{-1}$ and held there for 1 h in a tube furnace under an argon atmosphere. The activated sample was boiled in 0.1 M HCl for 1 h and then washed with copious deionized water to neutral.

**Synthesis of sGNS/cMWCNT/PANI Nanocomposite.** sGNS derived from GO was prepared as described in the literature,[33] and cMWCNT was prepared via an acid treatment of MWCNT[53] (diameter of 10−20 nm). The sGNS/cMWCNT/PANI nanocomposite was synthesized by an interfacial polymerization method. The typical procedure was as follows: sGNS (21 mg) and cMWCNT (9 mg) were added into a mixed solution of 20 mL of isopropyl alcohol and 100 mL of 1 M $H_2SO_4$, and the mixture was sonicated for 15 min to obtain a well-dispersed suspension. Then ammonium persulfate (APS, 0.76 g) was dissolved in the above solution to form a water phase. Aniline monomers (0.465 g) were dissolved in 100 mL of dichloromethane to form an oil phase. The water and oil phases were then carefully transferred to a 600 mL beaker. The reaction was performed at 0 °C for 24 h, and the resulting product was filtered, washed with deionized water and ethanol several times, and then dried at 60 °C under a vacuum to obtain the sGNS/cMWCNT/PANI nanocomposite. For comparison, sGNS/PANI and cMWCNT/PANI nanocomposites were synthesized through a procedure similar to that above without the presence of cMWCNT or sGNS, respectively (Table S1 in the Supporting Information, SI).

**Characterization.** The morphologies of the samples were analyzed by field-emission scanning electron microscopy (FESEM; Hitachi S4800, 30 kV) and transmission electron microscopy (TEM; JEOL JEM-1400, 200 kV). Fourier transform infrared (FTIR) spectroscopy was performed on a Nicolet 5700 spectrometer using KBr sample pellets. Raman spectroscopy was recorded with a Renishaw inVia +Reflex using a 50 mW He−Ne laser. X-ray photoelectron spectroscopy (XPS) analysis was carried on an ESCALAB 250Xi instrument with a monochromatic Al Ka X-ray source (1486.6 eV). X-ray diffraction (XRD) data were collected from 3° to 70° ($2\theta$ angle) from a Rigaku D/Max 2550 VB/PC X-ray diffractometer using Cu K$\alpha$ radiation. Nitrogen adsorption−desorption isotherms were performed using a Micromeritics ASAP 2020 analyzer at 77 K. Before measurements, the samples were degassed in a vacuum at 473 K for 8 h. The specific surface area and pore-size distribution were calculated using the BET and slit/cylindrical nonlocal density functional theory (NLDFT) methods, respectively. The UV−vis spectra were obtained using a Shimadzu UV-2102PC spectrophotometer.

**Electrochemical Measurements.** The sGNS/cMWCNT/PANI cathode was prepared by mixing active material, acetylene black, and poly(tetrafluoroethylene) (PTFE) in a mass ratio of 85:10:5 to form a homogeneous slurry. Then the slurry was rolled and pressed onto the titanium mesh and dried at 120 °C for 3 h. The aGNS anode was prepared through a similar procedure by mixing 95 wt % aGNS and 5 wt % PTFE. To fabricate an ASC device, the loading mass ratio of active materials (aGNS:sGNS/cMWCNT/PANI) was estimated to be 3.2 from the specific capacitance in terms of their charge−discharge curves in a three-electrode cell, in which platinum foil and Ag/AgCl electrodes were applied as counter and reference electrodes, respectively. The ASC was constructed with a glassy fibrous separator (Scheme 1) and performed in a two-electrode cell in a 1 M aqueous $H_2SO_4$ electrolyte.

Cyclic voltammetry (CV), galvanostatic charge−discharge, and electrochemical impedance spectroscopy (EIS) were carried out by a CHI760D electrochemical workstation, and the cycling stability of the ASC device was conducted on a LAND CT2001A program testing system. Data analysis of the electrochemical measurements is shown in the SI.

## RESULTS AND DISCUSSION

**Negative Electrode Materials.** FESEM and high-resolution TEM (HRTEM) were used to characterize the microstructures of GNS and aGNS. As shown in Figure 1a, GNS displays an unsmooth surface with lots of up-and-down undulations, deriving from a large volume expansion in the foaming process. The high-magnification image further confirms the loose architecture of GNS, where GNS exists in a few-layer-stacked structure (Figure 1b). The large space between the GNS layers is related to the intercalation of SA molecules into GNS and the release of phenol and $CO_2$ during thermal reduction (illustrated in Scheme 2). Figure 1c shows

**Scheme 2. Schematic Diagram for Thermal Decomposition of SA**

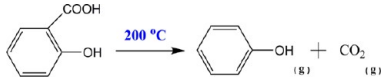


that the surface of aGNS is crumpled and curved, exhibiting the key feature of well-exfoliated thin sheets. HRTEM (Figure 1d) demonstrates a porous structure of aGNS with a size ranging from ∼1 to 7 nm (some are indicated by red arrows), which is attributed to the KOH etch on the surface of GNS. The activation of GNS with KOH proceeds as $6KOH + C \leftrightarrow 2K + 3H_2 + 2K_2CO_3$, followed by decomposition of $K_2CO_3$ and reaction of $K/K_2CO_3/CO_2$ with carbon. The etched nanopores of aGNS are highly expected to improve the electrochemical performance compared to chemically reduced graphene.[7]

To investigate the structures of GNS and aGNS, FTIR, XPS, XRD, and Raman spectroscopy were employed. Compared to GO, the characteristic peaks of the oxygen groups[54] at 1724, 1384, 1260, and 1064 $cm^{-1}$ are markedly weakened in GNS and aGNS (Figure 2a), indicating that GO is successfully reduced in a mixed gas flow of hydrogen and argon (20:80, v/v). Meanwhile, the C═C stretching vibration of aGNS is red-shifted to 1552 $cm^{-1}$ compared to 1565 $cm^{-1}$ of GNS, implying that $\pi$ conjugation is further restored under an elevated temperature of 800 °C. The electric conjugation of GNS and aGNS is further studied by XPS analysis. As shown in Figure 2b, the C 1s peak is deconvoluted at 284.6, 285.6, 286.7, and 288.2 eV, corresponding to C═C in the aromatic rings and C−OH, C−O−C, and C═O groups, respectively.[55] It is found that the amounts of the C−OH, C−O−C, and C═O groups in aGNS decrease and the content of $sp^2$-bonded carbon increases by 10.3% compared with that in GNS (Table S2 in the SI), indicating a higher $\pi$-conjugation degree for aGNS. Figure 2c shows the XRD patterns of GO, GNS, and aGNS. GO exhibits a sharp diffraction peak at $2\theta$ = 11.6°, corresponding to the diffraction of the (001) plane[7] with an interlayer distance of 0.76 nm. For GNS and aGNS, a broad peak of the (002) plane centered at $2\theta$ = 25° is observed. aGNS presents a much weaker peak compared to GNS, suggesting the increased disorder of aGNS sheets, which can be attributed to the porous structure induced by KOH activation. The structural change after activation is further reflected in the Raman spectra (Figure 2d). All the spectra of GO, GNS, and aGNS display the existence of D and G bands located at 1350−1356 and 1593−1604 $cm^{-1}$, respectively. The intensity ratio of the D and G bands ($I_D/I_G$) calculated from the band area is 1.25 in GO and increases to 1.62 in GNS and 1.30 in aGNS. The larger value of $I_D/I_G$ for GNS demonstrates a higher degree of disorder, which may be ascribed to the massive structural defects introduced by ultrasonic exfoliation and the foaming process. Noticeably, the value of $I_D/I_G$ for aGNS is much lower than that of GNS, suggesting that the restoration of $sp^2$-hybridized carbon is dominant in the activation process, although some new structural defects are introduced.

Figure 3 displays the nitrogen adsorption−desorption isotherms of the samples and the results of the pore-size distribution based on a hybrid NLDFT. Compared to GNS,

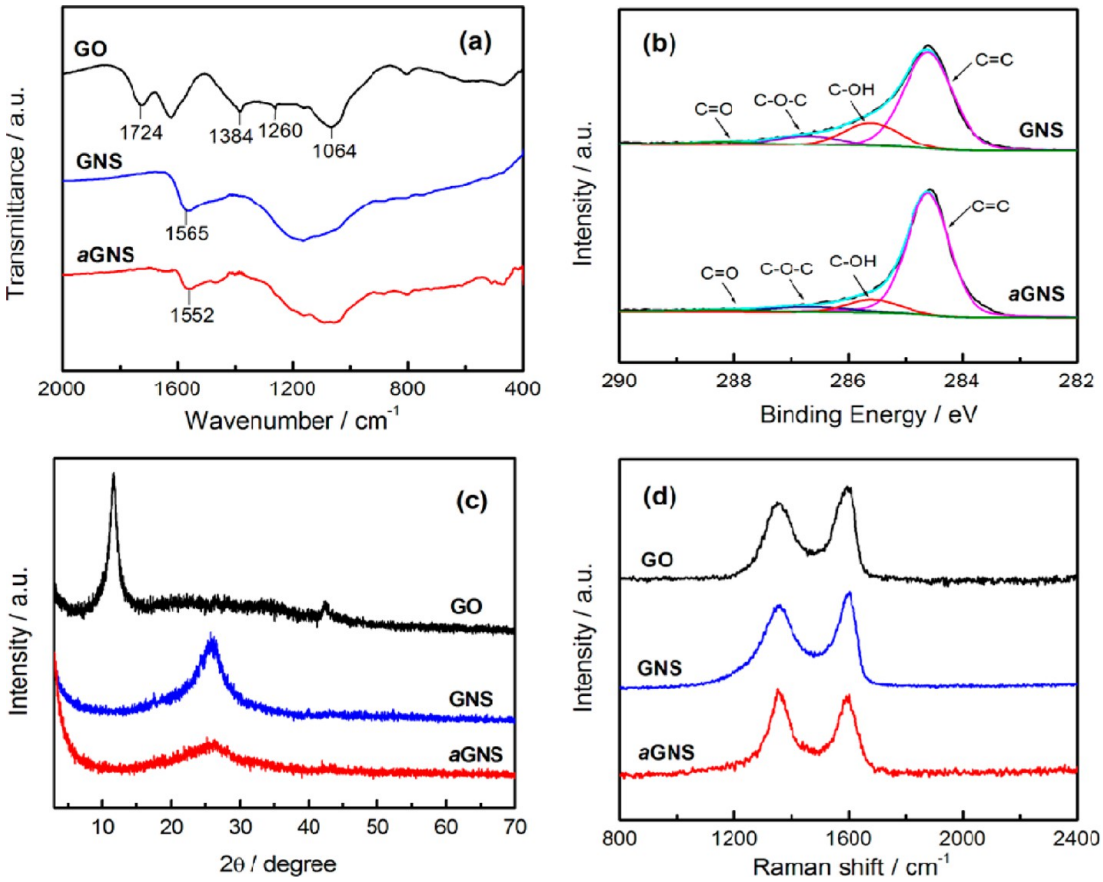


**Figure 2.** (a) FTIR, (b) XPS, (c) XRD, and (d) Raman spectra of GO, GNS, and aGNS.

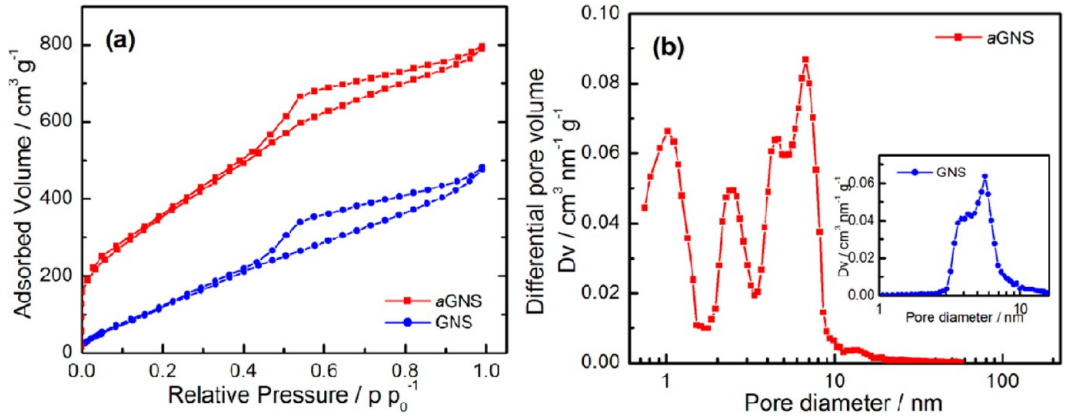


**Figure 3.** (a) Nitrogen adsorption−desorption isotherms and (b) corresponding pore-size distributions of GNS and aGNS.

aGNS shows a strong nitrogen adsorption below the relative pressure of 0.1 (Figure 3a), which is a typical feature of micropore filling.[52] The distinct hysteresis loop in the range of 0.4−1.0 $P/P_0$ for both samples suggests the presence of mesopores, revealing the textural porosity of graphene due to the rough sheet surface, which is in accordance with the FESEM observation (Figure 1). The pore-size distribution of aGNS shows a sharp peak around 1 nm for micropores with another narrow peak in the ∼2.5 nm size range as well as mesopores centered around 6.7 nm (Figure 3b). The BET surface area of *a*GNS is 1383 $m^2\ g^{-1}$ with a total pore volume of 1.2 $cm^3\ g^{-1}$, much higher than that of GNS (682 $m^2\ g^{-1}$, 0.72 $cm^3\ g^{-1}$). Such an intriguing feature of aGNS is very beneficial for the transport and diffusion of hydrated ions (0.6−0.76 nm) during the fast charging/discharging process,[46] thus resulting in an enhanced electrochemical performance.

Figure 4 reflects the electrochemical performance of the GNS and aGNS electrodes in a three-electrode cell. The aGNS electrode exhibits an ideal rectangular CV curve, while GNS deviates from the rectangular shape (Figure 4a). The deviation of the CV shape of GNS may be ascribed to the unfavorable accessibility between the GNS electrode and $H_2SO_4$ electrolyte, which is caused by the poor wettability of GNS in an aqueous $H_2SO_4$ electrolyte (Figure S1 in the SI). Moreover, aGNS still presents a relatively rectangular CV shape even at a fast sweeping rate of 200 mV $s^{-1}$ (Figure 4b), implying very


dx.doi.org/10.1021/am4028235 | ACS Appl. Mater. Interfaces 2013, 5, 8467−8476

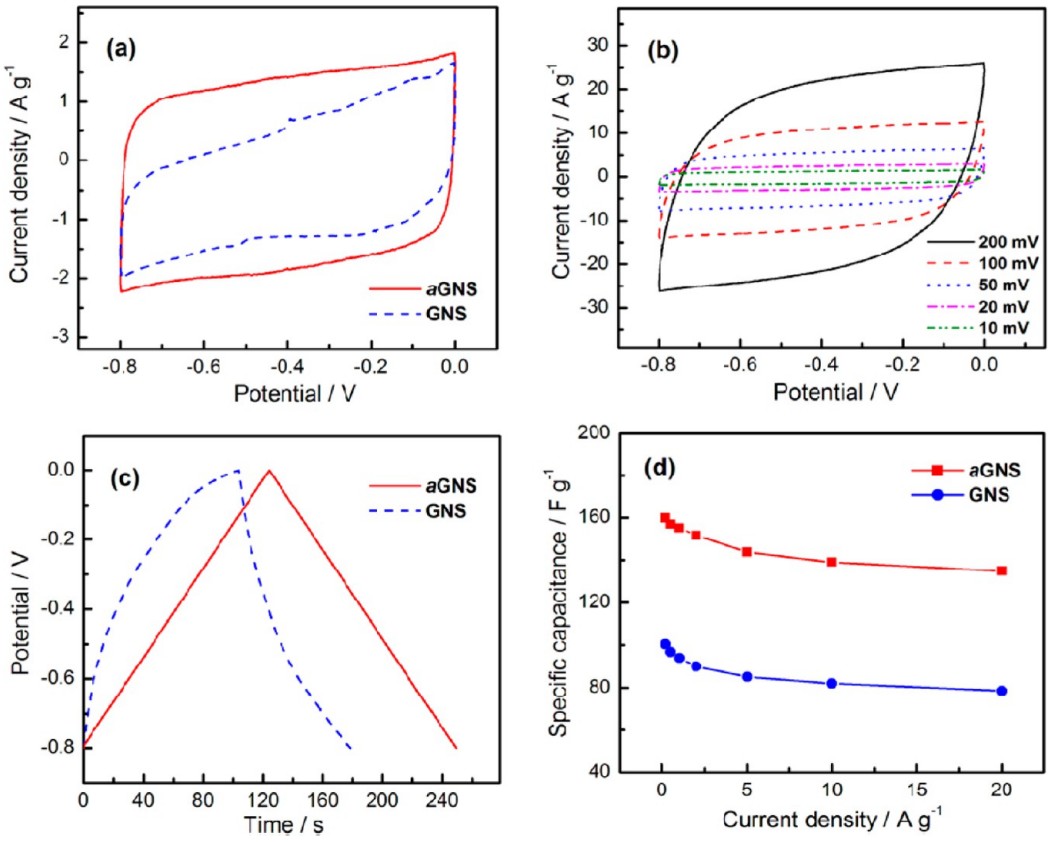


**Figure 4.** (a) CV curves of GNS and aGNS at 10 mV $s^{-1}$ in a 1 M $H_2SO_4$ solution. (b) CV curves of aGNS at different scan rates. (c) Galvanostatic charge−discharge curves of GNS and aGNS at a current density of 1 A $g^{-1}$. (d) Specific capacitances as a function of the various current densities of the GNS and aGNS electrodes.

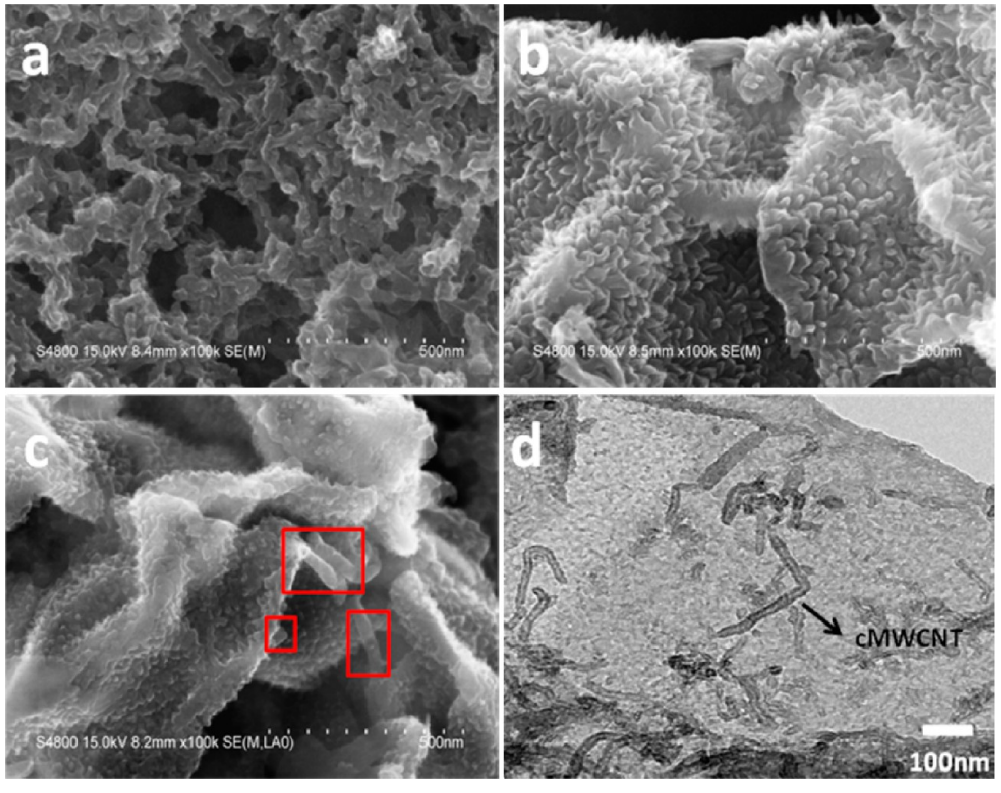


**Figure 5.** FESEM images of (a) cMWCNT/PANI, (b) sGNS/PANI, and (c) sGNS/cMWCNT/PANI. (d) TEM image of sGNS/cMWCNT/PANI.


dx.doi.org/10.1021/am4028235 | ACS Appl. Mater. Interfaces 2013, 5, 8467−8476

efficient charge transfer and electrolyte diffusion within the porous aGNS electrode. aGNS displays a triangular shape of the charge−discharge plots (Figure 4c), indicating a typical characteristic of electric double-layer capacitance. However, the curve of GNS is fairly nonlinear and asymmetric, consistent with disproportionation of the CV shape. Furthermore, no apparent IR drop in the curve is observed for aGNS, meaning that the electrode has a low internal resistance. Figure 4d demonstrates that aGNS not only owns a higher specific capacitance but also maintains a better rate capacity compared to GNS. With the current density increasing from 0.2 to 20 A $g^{-1}$, the capacitance of aGNS only decreases from 160 to 135 F $g^{-1}$. This may be attributed to the sufficient contact between the electrolyte ions and active materials of the aGNS electrode, which further confirms the superiority of the porous aGNS. Furthermore, the aGNS electrode also demonstrates a superior electrochemical performance over the cMWCNT and sGNS electrodes (see Figure S2 and Table S3 in the SI).

**Positive Electrode Materials.** To study the microstructures of cMWCNT/PANI, sGNS/PANI, and sGNS/cMWCNT/PANI, FESEM and TEM were employed. The FESEM image of cMWCNT/PANI shows that PANI is coarsely coated on the surface of cMWCNT and the thickness of the PANI layer is about 10 nm (Figure 5a). For the sGNS/PANI composite, PANI nanorods are vertically aligned on the surface of sGNS with an average diameter of 10−20 nm (Figure 5b). As shown in Figure 5c, the FESEM image of sGNS/cMWCNT/PANI demonstrates a coexisting structure of sGNS-supported PANI nanorod arrays and coaxial cMWCNT/PANI nanocables in sGNS/cMWCNT/PANI. The cMWCNT sandwiched between sGNS greatly restrains the aggregation of sGNS, leading to an enhanced surface area for depositing PANI. Thus, sGNS/cMWCNT/PANI has a higher load mass of PANI (43.1%) than sGNS/PANI (31.9%) and cMWCNT/PANI (22.7%). The TEM image (Figure 5d) further indicates the coexisting structures of the cMWCNT/PANI nanocables and sGNS-supported PANI nanorod arrays with diameters of 10−20 nm (the black spots).

Figure 6 shows the FTIR, Raman and UV−vis spectra of cMWCNT/PANI, sGNS/PANI, and sGNS/cMWCNT/PANI. All of the samples exhibit the main IR bands similar to that of PANI in 1560−1570, 1480−1500, and 1290−1300 $cm^{-1}$.[33] Compared to cMWCNT/PANI (1569 and 1495 $cm^{-1}$) and sGNS/PANI (1566 and 1488 $cm^{-1}$), the C=C stretching vibrations of the quinoid and benzenoid rings in sGNS/cMWCNT/PANI shift to lower wavenumbers (1561 and 1482 $cm^{-1}$), indicating an enhancement of $\pi$ conjugation between the PANI chains and sGNS/cMWCNT substrate. In Raman spectra (Figure 6b), the C=C stretch (1499 $cm^{-1}$) and in-plane C−H bending (1161 $cm^{-1}$) of benzenoid rings in sGNS/cMWCNT/PANI shift to lower wavenumbers compared with the binary composites, which also demonstrates that PANI exhibits the highest conjugated degree in the ternary composite. The conjugated degree of PANI is further revealed by UV−vis analysis (Figure 6c). For cMWCNT/PANI and sGNS/PANI, the absorption peaks at 799 and 848 nm can be assigned to the $\pi$-polaron transition, which is a typical characterization of doped PANI.[40,56] Compared with the binary composites, a red shift of the $\pi$-polaron transition to 857 nm is observed in sGNS/cMWCNT/PANI, indicating an increase of the conjugated degree of PANI in the ternary composite. This result is consistent with our FTIR and Raman analysis. The enhancement of the conjugated degree is related to the larger

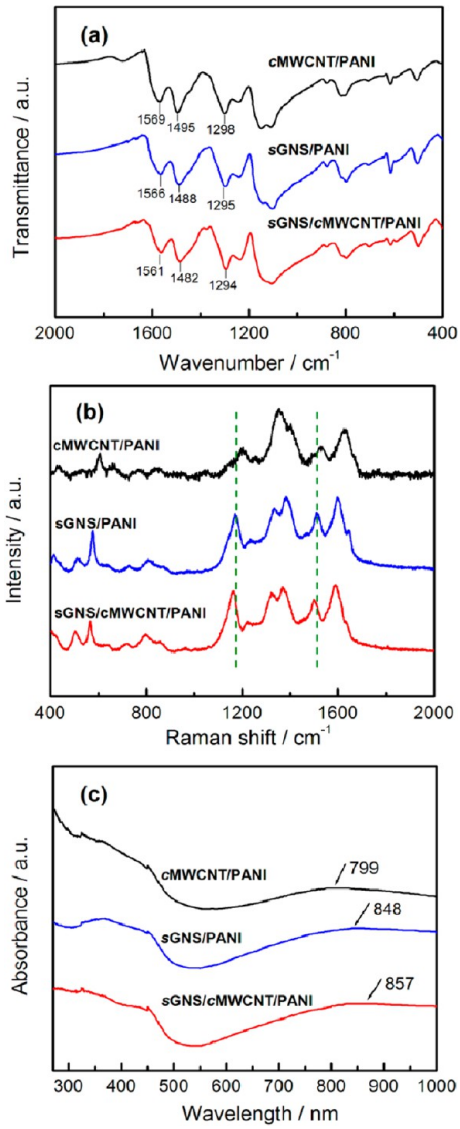


**Figure 6.** (a) FTIR, (b) Raman, and (c) UV−vis spectra of cMWCNT/PANI, sGNS/PANI, and sGNS/cMWCNT/PANI.

specific surface of sGNS/cMWCNT (1391 $m^2$ $g^{-1}$) compared with those of cMWCNT and sGNS (538 and 1044 $m^2$ $g^{-1}$) for depositing PANI (Figure S3 in the SI). Moreover, the higher degree of conjugation is beneficial to relatively low internal resistance, which is also confirmed from the Nyquist plots in Figure 7b.

The capacitive performance of sGNS/PANI, cMWCNT/PANI, and sGNS/cMWCNT/PANI was evaluated by CV, galvanostatic charge−discharge, and EIS in a three-electrode system. Figure 7a shows the CV curves of the samples at a scan rate of 5 mV $s^{-1}$ in a 1 M $H_2SO_4$ solution. All of the composites present two pairs of redox peaks ($C_1/A_1$ and $C_2/A_2$), corresponding to the leucoemeraldine/emeraldine and emeraldine/pernigraniline structural conversions, which indicates good pseudocapacitance characteristics.[57] It is also seen that sGNS/cMWCNT/PANI possesses a larger CV curve area than binary composites, relating to its higher capacitance. Figure 7b depicts the Nyquist plots measured at frequencies of 100 kHz to 0.01 Hz. It is found that all composite electrodes show nearly vertical lines along the imaginary axis in the low-frequency region, indicating an ideally capacitive behavior due to the fast


dx.doi.org/10.1021/am4028235 | ACS Appl. Mater. Interfaces 2013, 5, 8467−8476

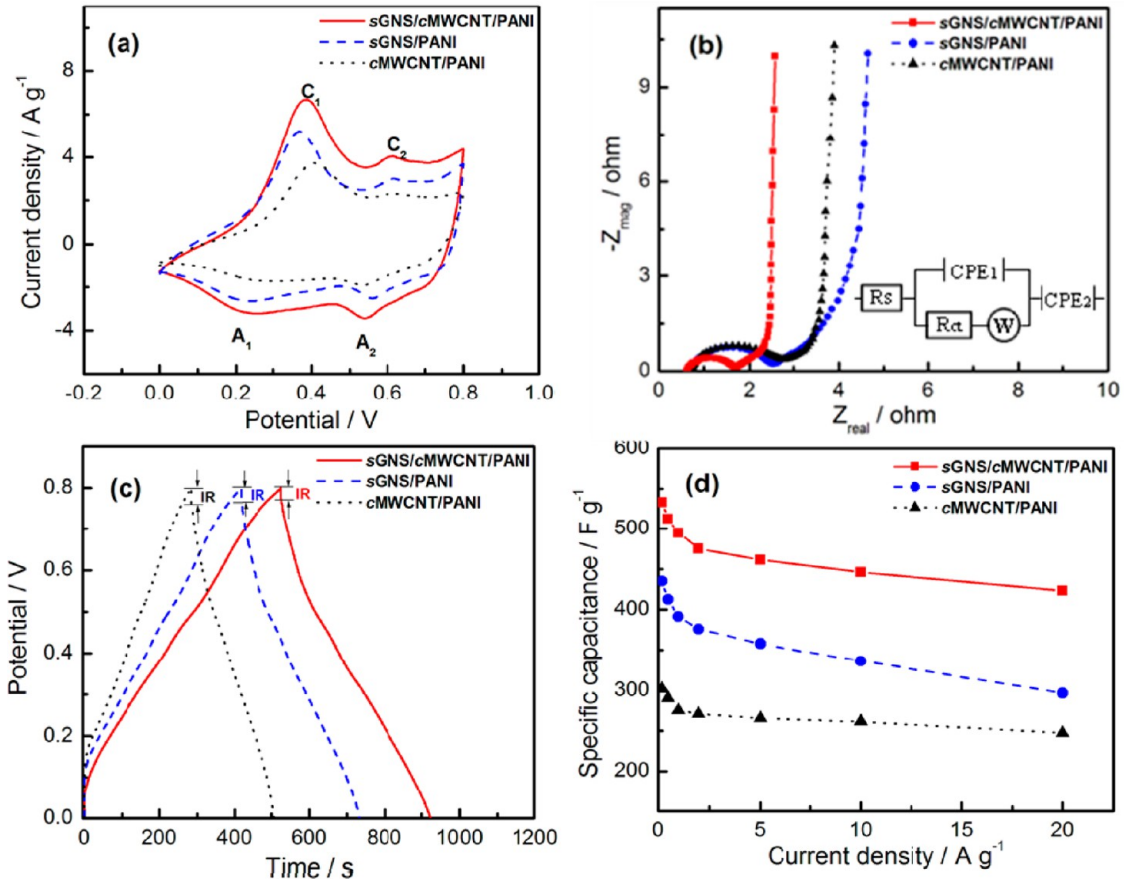


**Figure 7.** Electrochemical performance of cMWCNT/PANI, sGNS/PANI, and sGNS/cMWCNT/PANI in a 1 M $H_2SO_4$ solution. (a) CV curves at a scan rate of 5 mV $s^{-1}$. (b) Nyquist plots in the frequency range of 100 kHz to 0.01 Hz and the equivalent circuit obtained from fitting impedance spectra. (c) Galvanostatic charge−discharge curves at a current density of 1 A $g^{-1}$. (d) Specific capacitances as a function of the various current densities.

and reversible redox reaction of PANI nanolayers or nanorods on the nanocarbonaceous materials. In the high-frequency region, the intercept at the real axis represents the ohmic resistance ($R_s$) including the ionic resistance of the electrolyte, intrinsic resistance of the substrate, and contact resistance. The semicircle corresponds to the charge-transfer resistance ($R_{ct}$) at the electrode/electrolyte interface. It is apparent that sGNS/cMWCNT/PANI has much smaller $R_s$ (0.62 Ω) and $R_{ct}$ (0.99 Ω) than those of cMWCNT/PANI (0.73 and 1.97 Ω) and sGNS/PANI (0.71 and 1.76 Ω). To further understand the behavior of PANI composite electrodes, equivalent circuit modeling was established (Figure 7b, inset). Also, the values derived from fitting to the model are outlined in Table S4 in the SI, which agree well with the experimental data. As shown in Figure 7c, the charge−discharge curves present symmetrical and the mirror-like image, meaning that the redox reaction in the composites is reversible. It can be noted that the IR drop of sGNS/cMWCNT/PANI (0.0267 V) is lower than that of sGNS/PANI (0.038 V) and cMWCNT/PANI (0.039 V), implying that the energy consumed by internal resistance is reduced and therefore the effective energy storage is improved. Calculations based on the discharge curve indicate that sGNS/cMWCNT/PANI has a larger specific capacitance of 495 F $g^{-1}$, which is due to the higher PANI yield (Table S1 in the SI) and the unique interpenetrating structure. Moreover, sGNS/cMWCNT/PANI maintains 79.3% of the initial capacitance with growing current densities from 0.2 to 20 A $g^{-1}$ (Figure 7d), a little inferior to cMWCNT/PANI (81.9%), which is ascribed to the good conductivity of cMWCNT and the low PANI loading on cMWCNT. Despite the rate capability, sGNS/cMWCNT/PANI exhibits a more excellent electrochemical performance, thus leading to its selection as the positive electrode material.

**ASC.** Considering the high pseudocapacitance of the sGNS/cMWCNT/PANI composite and the fast charge-transport property of aGNS, an ASC was fabricated using sGNS/cMWCNT/PANI and aGNS as the positive and negative electrodes (Scheme 1), respectively. For supercapacitors, it is well-known that the charge balance between the positive and negative electrodes will follow the relationship $q^+ = q^-$, where the stored charges are related to the specific capacitance ($C$), the potential window ($\Delta V$), and the mass of the electrode ($m$) according to $q = C\Delta Vm$.[14] Therefore, the optimal mass ratio between the electrodes (aGNS:sGNS/cMWCNT/PANI) should be 3.2 in the present ASC device. Figure 8a shows the CV curves of the as-fabricated ASC device, with different operating potential windows varying from 0−0.8 to 0−1.8 V. It is noted that the as-fabricated ASC exhibits a good capacitive behavior with quasi-rectangular CV curves even at a voltage up to 1.6 V. However, the CV curve operated at 0−1.8 V deviates seriously from rectangularity, which may be attributed to the polarization intensifying as a result of decomposition of PANI. Interestingly, unlike the sGNS/cMWCNT/PANI single electrode, the sGNS/cMWCNT/PANI//aGNS supercapacitor


dx.doi.org/10.1021/am4028235 | ACS Appl. Mater. Interfaces 2013, 5, 8467−8476

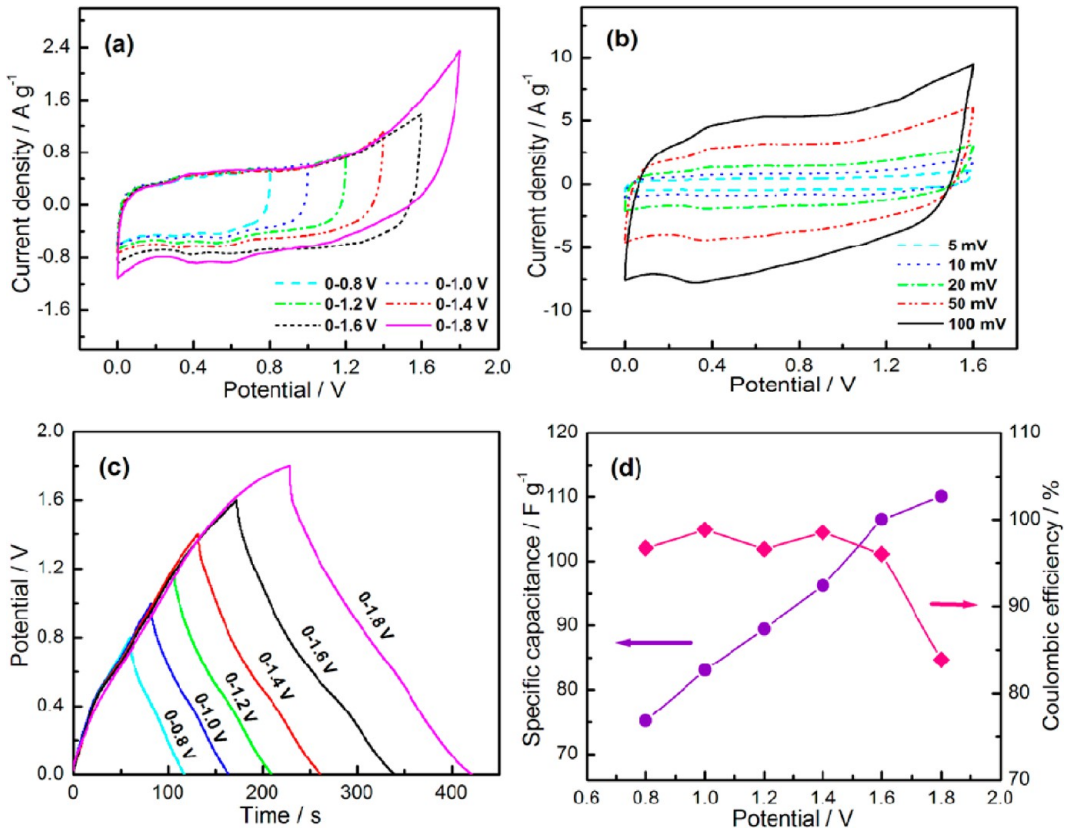


**Figure 8.** Capacitive performances of the sGNS/cMWCNT/PANI//aGNS ASC in a 1 M $H_2SO_4$ solution. (a) CV curves measured at different potential windows at a scan rate of 5 mV $s^{-1}$. (b) CV curves at different scan rates with a maximum potential window of 1.6 V. (c) Galvanostatic charge−discharge curves at a current density of 1 A $g^{-1}$. (d) Specific capacitances and Coulombic efficiencies as a function of the various potential windows.

shows a rather weak pair of redox peaks at around 0.4 V, suggesting the feeble faradaic reactions and the predominance of an electrical double-layer capacitance. Moreover, ASC retains a relatively rectangular CV shape even at a high scan rate of 100 mV $s^{-1}$ within 0−1.6 V cell voltage (Figure 8b), indicating the fast charge−discharge characteristic. Figure 8c depicts the galvanostatic charge−discharge curves of the as-fabricated ASC advice at a current density of 1 A $g^{-1}$. It is found that both the charge and discharge curves remain in good symmetry at a cell voltage as high as 1.6 V, revealing an excellent capacitive performance. Figure 8d shows the specific capacitance and Coulombic efficiency of the ASC device with an increase of the cell voltage. It is found that the capacitance of ASC increases significantly from 75 to 107 F $g^{-1}$ (based on the total mass of both electrodes) in a cell voltage from 0.8 to 1.6 V and then displays a slight increase with increasing cell voltage. Moreover, the Coulombic efficiency remains above 95% within a operation potential of 0.8−1.6 V. However, when the cell voltage is above 1.6 V, the Coulombic efficiency decreases evidently, which might be ascribed to decomposition of PANI. As a result, a cell voltage of 1.6 V is chosen for further investigation of the overall electrochemical performance of the ASC device.

Figure 9 shows the Ragone plots (energy density vs power density) of symmetric supercapacitors and an ASC device based on sGNS/cMWCNT/PANI and aGNS. It is clearly seen that the as-fabricated ASC device displays much higher energy and power densities than the symmetric supercapacitors. The sGNS/cMWCNT/PANI//aGNS ASC with a potential window of 1.6 V can exhibit an energy density of 41.5 Wh $kg^{-1}$ and a

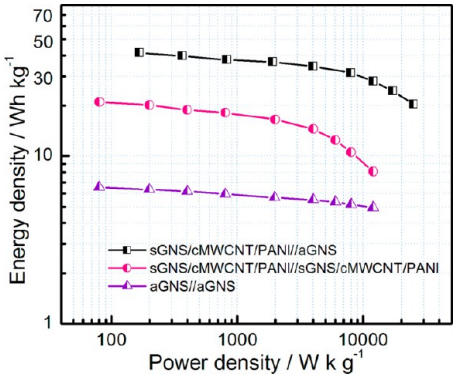


**Figure 9.** Ragone plots of asymmetric and symmetric supercapacitors based on sGNS/cMWCNT/PANI and aGNS electrodes.

power density of 167 W $kg^{-1}$ at a current density of 0.2 A $g^{-1}$ and still maintains 20.4 Wh $kg^{-1}$ at a power density of 25.0 kW $kg^{-1}$. In contrast, the supercapacitors with symmetric aGNS and sGNS/cMWCNT/PANI electrodes deliver much lower energy densities of 6.5 and 21.1 Wh $kg^{-1}$ at a current density of 0.2 A $g^{-1}$, respectively. In addition, the energy density of the as-fabricated ASC based on sGNS/cMWCNT/PANI and aGNS is also comparable to that of majority ASC devices reported in recent years such as the graphene/$RuO_2$//graphene/PANI ASC (6.8 Wh $kg^{-1}$; 49.8 kW $kg^{-1}$),[5] Ni(OH)$_2$/graphene//porous graphene ASC (13.5 Wh $kg^{-1}$; 15.2 kW $kg^{-1}$),[14] $MnO_2$//graphene hydrogel ASC (14.9 Wh $kg^{-1}$; 10.0 kW $kg^{-1}$),[15] $MnO_2$//mesoporous carbon nanotubes ASC (10.4 Wh


dx.doi.org/10.1021/am4028235 | ACS Appl. Mater. Interfaces 2013, 5, 8467−8476

$kg^{-1}$; 2 kW $kg^{-1}$),[58] graphene/$MnO_2$//activated carbon nanofiber ASC (8.2 Wh $kg^{-1}$; 16.5 kW $kg^{-1}$),[59] and activated carbon//$K_{0.27}MnO_2{\cdot}0.6H_2O$ ASC (17.6 Wh $kg^{-1}$; 2 kW $kg^{-1}$).[60] The high-energy electrochemical behavior of sGNS/cMWCNT/PANI//aGNS ASC can be ascribed to the following factors. First, the excellent interfacial contact between the PANI nanorods or nanolayer and sGNS/cMWCNT substrate through $\pi-\pi$ interaction greatly increases the utilization of PANI and shortens the diffusion and migration paths for electrolyte ions during rapid redox reaction, thus leading to the high energy density of the ASC device. Second, the unique interpenetrating architecture of sGNS/cMWCNT/PANI effectively increases the accessible contact area for rapid charge transport at the electrolyte/electrode interface, hence improving the electrochemical performance of the positive electrode. Third, the aGNS with a flexible porous structure is favorable for large electric double-layer capacitance and fast hydrate ion transport, providing both enhanced energy storage and good rate capability.

The cycling stability of the as-fabricated ASC is carried out by repeating the galvanostatic charge−discharge test within 0−1.6 V at a current density of 1 A $g^{-1}$ (Figure 10). The as-fabricated ASC device exhibits an excellent electrochemical stability with only 2.6% deterioration of the initial specific capacitance after 1000 cycles, and the capacitance retention still keeps 91.4% after 5000 cycles. Such cycling performance is superior to those of other ASC devices, such as the graphene/$MnO_2$//activated carbon nanofiber ASC (97.3% retention after 1000 cycles),[59] $MnO_2$/aMEGO//aMEGO ASC (80.4% retention after 5000 cycles),[18] $MnO_2$//graphene hydrogel ASC (83.4% retention after 5000 cycles),[15] $Co(OH)_2$//activated carbon ASC (93% retention after 1000 cycles),[9] graphene/$RuO_2$//graphene/PANI ASC (70% retention after 2500 cycles),[5] and activated carbon//$LiTi_2(PO_4)_3$ ASC (85% retention after 1000 cycles).[10] The excellent cycling stability of the as-fabricated ASC is possibly attributed to three aspects. First, the PANI nanorods or nanolayer in the sGNS/cMWCNT/PANI composite greatly relieve the volumetric changes of PANI during the charge−discharge process owing to a small size effect. Second, the $\pi-\pi$ interaction between the PANI loading and sGNS/cMWCNT substrate supplies good elasticity to accommodate the strain of the volumetric change. Finally, the synergetic effects of both the sGNS/cMWCNT/PANI composite and porous aGNS electrodes contribute to the enhanced cycling performance.

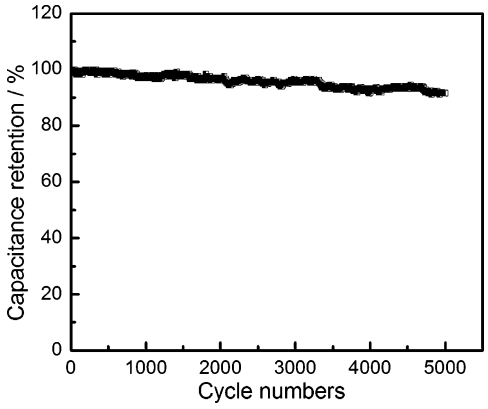


**Figure 10.** Cycle performance of the sGNS/cMWCNT/PANI//aGNS ASC device.

## CONCLUSION

A novel and durable ASC device based on hierarchical sGNS/cMWCNT/PANI nanocomposite with an interpenetrating network as the positive electrode and aGNS with porous structure as the negative electrode has been successfully developed in an aqueous $H_2SO_4$ solution. After optimization, the as-assembled ASC can be reversibly charged/discharged in a wide voltage region of 0−1.6 V and exhibits a preferable specific capacitance of 107 F $g^{-1}$ at a current density of 1 A $g^{-1}$. The remarkable energy density of 20.5 Wh $kg^{-1}$ (25 kW $kg^{-1}$) and the stable cycling performance with 91% capacitance retention after 5000 cycles is competitive to most of the other ASC devices reported previously. We believe a more appropriate negative electrode with suitable potential and matchable capacitance will further improve the performance of as-assembled ASC. These encouraging findings can open up the possibility of conducting polymer-based ASC in high-performance energy storage applications.

## ASSOCIATED CONTENT

### Supporting Information

Preparation of sGNS and cMWCNT, synthesis conditions and characterization for PANI composites, data analysis of electrochemical measurements, MB technique for specific surface area measurement, component intensities and wetting dispersibility of GNS and aGNS, and electrochemical performance of aGNS, sGNS, and cMWCNT. This material is available free of charge via the Internet at http://pubs.acs.org.

## AUTHOR INFORMATION

### Corresponding Author

*Tel.: +86-21-64253527 E-mail: gengchaow@ecust.edu.cn.

### Notes

The authors declare no competing financial interest.

## ACKNOWLEDGMENTS

We greatly appreciate financial support of the National Natural Science Foundation of China (Grant 51173042), Shanghai Municipal Science and Technology Commission (Grant 12nm0504102), Fundamental Research Funds for the Central Universities, and Innovation Program of Shanghai Municipal Education Commission (Grant 11ZZ55).

## REFERENCES

(1) Miller, J. R.; Simon, P. *Science* **2008**, *321*, 651−652.
(2) Simon, P.; Gogotsi, Y. *Nat. Mater.* **2008**, *7*, 845−854.
(3) Lee, S. W.; Gallant, B. M.; Byon, H. R.; Hammond, P. T.; Shao-Horn, Y. *Energy Environ. Sci.* **2011**, *4*, 1972−1985.
(4) Liu, C.; Li, F.; Ma, L. P.; Cheng, H. M. *Adv. Mater.* **2010**, *22*, E28−E62.
(5) Zhang, J. T.; Jiang, J. W.; Li, H. L.; Zhao, X. S. *Energy Environ. Sci.* **2011**, *4*, 4009−4015.
(6) Izadi-Najafabadi, A.; Yasuda, S.; Kobashi, K.; Yamada, T.; Futaba, D. N.; Hatori, H.; Yumura, M.; Iijima, S.; Hata, K. *Adv. Mater.* **2010**, *22*, E235−E241.
(7) Zhu, Y. W.; Murali, S.; Stoller, M. D.; Ganesh, K. J.; Cai, W. W.; Ferreira, P. J.; Pirkle, A.; Wallace, R. M.; Cychosz, K. A.; Thommes, M.; Su, D.; Stach, E. A.; Ruoff, R. S. *Science* **2011**, *332*, 1537−1541.
(8) El-Kady, M. F.; Strong, V.; Dubin, S.; Kaner, R. B. *Science* **2012**, *335*, 1326−1330.
(9) Luo, J. Y.; Xia, Y. Y. *J. Power Sources* **2009**, *186*, 224−227.

(10) Kong, L. B.; Liu, M.; Lang, J. W.; Luo, Y. C.; Kang, L. *J. Electrochem. Soc.* **2009**, *156*, A1000−A1004.
(11) Algharaibeh, Z.; Liu, X. R.; Pickup, P. G. *J. Power Sources* **2009**, *187*, 640−643.
(12) Qu, Q. T.; Zhang, P.; Wang, B.; Chen, Y. H.; Tian, S.; Wu, Y. P.; Holze, R. *J. Phys. Chem. C* **2009**, *113*, 14020−14027.
(13) Tang, Z.; Tang, C. H.; Gong, H. *Adv. Funct. Mater.* **2012**, *22*, 1272−1278.
(14) Yan, J.; Fan, Z. J.; Sun, W.; Ning, G. Q.; Wei, T.; Zhang, Q.; Zhang, R. F.; Zhi, L. J.; Wei, F. *Adv. Funct. Mater.* **2012**, *22*, 2632−2641.
(15) Gao, H. C.; Xiao, F.; Ching, C. B.; Duan, H. W. *ACS Appl. Mater. Interfaces* **2012**, *4*, 2801−2810.
(16) Wang, D. W.; Li, F.; Cheng, H. M. *J. Power Sources* **2008**, *185*, 1563−1568.
(17) Du, X.; Wang, C. Y.; Chen, M. M.; Jiao, Y.; Wang, J. *J. Phys. Chem. C* **2009**, *113*, 2643−2646.
(18) Zhao, X.; Zhang, L. L.; Murali, S.; Stoller, M. D.; Zhang, Q. H.; Zhu, Y. W.; Ruoff, R. S. *ACS Nano* **2012**, *6*, 5404−5412.
(19) Qu, Q. T.; Shi, Y.; Li, L. L.; Guo, W. L.; Wu, Y. P.; Zhang, H. P.; Guan, S. Y.; Holze, R. *Electrochem. Commun.* **2009**, *11*, 1325−1328.
(20) Eom, J. Y.; Jung, I. H.; Lee, J. H. *J. Power Sources* **2011**, *196*, 9810−9814.
(21) Cericola, D.; Novák, P.; Wokaun, A.; Kötz, R. *Electrochim. Acta* **2011**, *56*, 8403−8411.
(22) Ionica-Bousquet, C. M.; Munoz-Rojas, D.; Casteel, W. J.; Pearlstein, R. M.; Kumar, G. G.; Pez, G. P.; Palacin, M. R. *J. Power Sources* **2011**, *196*, 1626−1631.
(23) Wang, Y. G.; Li, H. Q.; Xia, Y. Y. *Adv. Mater.* **2006**, *18*, 2619−2623.
(24) Fan, L. Z.; Hu, Y. S.; Manier, J.; Adelhelm, P.; Smarsly, B.; Antonietti, M. *Adv. Funct. Mater.* **2007**, *17*, 3083−3087.
(25) Li, L. X.; Song, H. H.; Zhang, Q. C.; Yao, J. Y.; Chen, X. H. *J. Power Sources* **2009**, *187*, 268−274.
(26) Yan, J.; Wei, T.; Shao, B.; Fan, Z. J.; Qian, W. Z.; Zhang, M. L.; Wei, F. *Carbon* **2010**, *48*, 487−493.
(27) Zhang, K.; Zhang, L. L.; Zhao, X. S.; Wu, J. S. *Chem. Mater.* **2010**, *22*, 1392−1401.
(28) Liao, Y. Z.; Zhang, C.; Wang, X.; Li, X. G.; Ippolito, S. J.; Kalantar-Zadeh, K.; Kaner, R. B. *J. Phys. Chem. C* **2011**, *115*, 16187−16192.
(29) Hyder, M. N.; Lee, S. W.; Cebeci, F. C.; Schmidt, D. J.; Shao-Horn, Y.; Hammond, P. T. *ACS Nano* **2011**, *5*, 8552−8561.
(30) Su, F. B.; Poh, C. K.; Chen, J. S.; Xu, G. W.; Wang, D.; Li, Q.; Lin, J. Y.; Lou, X. W. *Energy Environ. Sci.* **2011**, *4*, 717−724.
(31) Wu, Q.; Xu, Y. X.; Yao, Z. Y.; Liu, A. R.; Shi, G. Q. *ACS Nano* **2010**, *4*, 1963−1970.
(32) Wang, H. L.; Hao, Q. L.; Yang, X. J.; Lu, L. D.; Wang, X. *Nanoscale* **2010**, *2*, 2164−2170.
(33) Ma, B.; Zhou, X.; Bao, H.; Li, X. W.; Wang, G. C. *J. Power Sources* **2012**, *215*, 36−42.
(34) Liu, J. H.; An, J. W.; Zhou, Y. C.; Ma, Y. X.; Li, M. L.; Yu, M.; Li, S. M. *ACS Appl. Mater. Interfaces* **2012**, *4*, 2870−2876.
(35) Wu, T. M.; Lin, Y. W.; Liao, C. S. *Carbon* **2005**, *43*, 734−740.
(36) Sivakkumar, S. R.; Kim, W. J.; Choi, J. A.; MacFarlane, D. R.; Forsyth, M.; Kim, D. W. *J. Power Sources* **2007**, *171*, 1062−1068.
(37) Meng, C. Z.; Liu, C. H.; Fan, S. S. *Electrochem. Commun.* **2009**, *11*, 186−189.
(38) Liao, Y. Z.; Zhang, C.; Zhang, Y.; Strong, V.; Tang, J. S.; Li, X. G.; Kalantar-zadeh, K.; Hoek, E. M. V.; Wang, K. L.; Kaner, R. B. *Nano Lett.* **2011**, *11*, 954−959.
(39) Yan, J.; Wei, T.; Fan, Z. J.; Qian, W. Z.; Zhang, M. L.; Shen, X. D.; Wei, F. *J. Power Sources* **2010**, *195*, 3041−3045.
(40) Lu, X. J.; Dou, H.; Yang, S. D.; Hao, L.; Zhang, L. J.; Shen, L. F.; Zhang, F.; Zhang, X. G. *Electrochim. Acta* **2011**, *56*, 9224−9232.
(41) Zhou, S. P.; Zhang, H. M.; Wang, X. H.; Li, J.; Wang, F. S. *RSC Adv.* **2013**, *3*, 1797−1807.
(42) Nuraje, N.; Su, K.; Yang, N. I.; Matsui, H. *ACS Nano* **2008**, *2*, 502−506.
(43) Stoller, M. D.; Ruoff, R. S. *Energy Environ. Sci.* **2010**, *3*, 1294−1301.
(44) Lee, C. G.; Wei, X. D.; Kysar, J. W.; Hone, J. *Science* **2008**, *321*, 385−388.
(45) Rao, C. N. R.; Sood, A. K.; Subrahmanyam, K. S.; Govindaraj, A. *Angew. Chem. Int. Ed.* **2009**, *48*, 7752−7778.
(46) Wu, Z. S.; Ren, W. C.; Wang, D. W.; Li, F.; Liu, B. L.; Cheng, H. M. *ACS Nano* **2010**, *4*, 5835−5842.
(47) Bai, H.; Xu, Y. X.; Zhao, L.; Li, C.; Shi, G. Q. *Chem. Commun.* **2009**, 1667−1669.
(48) Georgakilas, V.; Otyepka, M.; Bourlinos, A. B.; Chandra, V.; Kim, N.; Kemp, K. C.; Hobza, P.; Zboril, R.; Kim, K. S. *Chem. Rev.* **2012**, *112*, 6156−6214.
(49) Zhong, J.; Deng, J. J.; Mao, B. H.; Xie, T.; Sun, X. H.; Mou, Z. G.; Hong, C. H.; Yang, P.; Wang, S. D. *Carbon* **2012**, *50*, 321−341.
(50) Bissett, M. A.; Tsuji, M.; Ago, H. *J. Phys. Chem. C* **2013**, *117*, 3152−3159.
(51) Hummers, W. S.; Offeman, R. E. *J. Am. Chem. Soc.* **1958**, *80*, 1339−1341.
(52) Zhang, L. L.; Zhao, X.; Stoller, M. D.; Zhu, Y. W.; Ji, H. X.; Murali, S.; Wu, Y. P.; Perales, S.; Clevenger, B.; Ruoff, R. S. *Nano Lett.* **2012**, *12*, 1806−1812.
(53) Rosca, I. D.; Watari, F.; Uo, M.; Akaska, T. *Carbon* **2005**, *43*, 3124−3131.
(54) Park, S. H.; Bak, S. M.; Kim, K. H.; Jegal, J. P.; Lee, S. I.; Lee, J.; Kim, K. B. *J. Mater. Chem.* **2011**, *21*, 680−686.
(55) Zhu, C. Z.; Guo, S. J.; Fang, Y. X.; Dong, S. J. *ACS Nano* **2010**, *4*, 2429−2437.
(56) Xu, J. J.; Wang, K.; Zu, S. Z.; Han, B. H.; Wei, Z. X. *ACS Nano* **2010**, *4*, 5019−5026.
(57) Xu, L. Q.; Liu, Y. L.; Neoh, K. G.; Kang, E. T.; Fu, G. D. *Macromol. Rapid Commun.* **2011**, *32*, 684−688.
(58) Jiang, H.; Li, C. Z.; Sun, T.; Ma, J. *Nanoscale* **2012**, *4*, 807−812.
(59) Fan, Z. J.; Yan, J.; Wei, T.; Zhi, L. J.; Ning, G. Q.; Li, T. Y.; Wei, F. *Adv. Funct. Mater.* **2011**, *21*, 2366−2375.
(60) Qu, Q. T.; Li, L.; Tian, S.; Guo, W. L.; Wu, Y. P.; Holze, R. *J. Power Sources* **2010**, *195*, 2789−2794.